Fluid Modeling of a Nitrogen Atmospheric-Pressure Planar Dielectric Barrier Discharge Driven by a Realistic Distorted Sinusoidal Alternating Current Power Source

REGULAR PAPER

Fluid Modeling of a Nitrogen Atmospheric-Pressure Planar Dielectric Barrier Discharge Driven by a Realistic Distorted Sinusoidal Alternating Current Power Source

Kai-Wen Cheng[1], Chieh-Tsan Hung[1], Kun-Mo Lin[1], Yuan-Ming Chiu[1], Jong-Shinn Wu[1,2*], and Jen-Perng Yu[3]

[1]Department of Mechanical Engineering, National Chiao Tung University, Hsinchu 30010, Taiwan
[2]National Center for High-Performance Computing, National Applied Research Laboratories, Hsinchu 30076, Taiwan
[3]Department of Information Management, Ming Chuan University, Tauyuan 33348, Taiwan

One-dimensional self-consistent simulations of a parallel-plate atmospheric-pressure nitrogen dielectric barrier discharge (DBD) are presented. The DBD was driven by a realistic distorted-sinusoidal voltage power source with a frequency of 60 kHz. The simulated discharge currents are in quantitative agreement with experimental measurements. N_4^+ ions gain more of the input electric power than electrons, which is unlike most glow discharges. The densities of all charged and neutral species increase exponentially with increasing applied peak voltage in the range of 6.2–8.6 kV. The higher the permittivity of the dielectric material, the larger the discharge current and the longer the period of gas breakdown. In addition, the quantity of accumulated charges at each electrode increases with increasing permittivity of the dielectric material. Finally, the increase in dielectric thickness from 1.0 to 2.0 mm greatly reduces the densities of all species and also the plasma absorbed by the power.
© 2012 The Japan Society of Applied Physics

1. Introduction

Atmospheric-pressure dielectric barrier discharges (DBDs) have become increasingly popular because of their benefits advantages compared with low-pressure plasmas, including easy implementation, low operational cost without requiring vacuum equipment and the possibility of the production of homogeneous plasma. In particular, nitrogen DBD has received much experimental interest over the past decade because of its simplicity and potential applications in several disciplines. This type of discharge is widely used in numerous applications in the fields of pollution control and surface treatment among others.[1–3] Thus, understanding of the fundamental plasma physics of nitrogen DBD is important in further improving the use and design of nitrogen DBD sources through simulations which are efficient and low-cost.

Nitrogen DBD is usually operated at atmospheric pressure and driven by an AC high-voltage power source. The discharge is sustained in the space between two electrodes covered with insulating dielectric materials. Generally, nitrogen DBD has been classified into two discharge forms: homogeneous and filamentary. Previous studies have shown that the type of DBD structure strongly depends on the operating conditions, such as the waveform, magnitude and frequency of applied voltage, type of dielectric material and gap distance between electrodes, among others.[4–10] In addition to experimental diagnostics, fluid modeling has been proved to be a very useful and cost-effective tool for classifying the atmospheric-pressure plasma physics and chemistry of nitrogen discharges.[11] However, prior to massive simulations of some specific nitrogen DBD, validation against experimental data is also very important for the correct interpretation of the underlying plasma physics and chemistry.

The fluid model consists of continuity equations, momentum equations, and energy equation for charged and neutral species coupled with the Poisson's electrostatic equation for the distribution of an electric field in a discharge. Most of them employed the simple local field approximation (LFA), which assumes that the input electrical energy is balanced by the local ionization energy, to replace the complete electron energy density equation.[5,6,8] Recently, Grubert *et al.*[12] have shown that the local mean energy approximation (LMEA), which includes the electron energy density equation in fluid modeling, generally produces more reasonable simulation results than experimental data in low-pressure glow discharge plasma. Although we are concerned with atmospheric discharge in this study, we decided to employ the LMEA in our fluid modeling for possible wide-range applications in the future.

In addition, there are abundant vibrationally excited nitrogen species in typical nitrogen DBD.[13] Consideration of the superelastic definition (e-V) collisions between an electron and vibrationally excited nitrogen becomes necessary in the model because they strongly affects electron energy distribution function (EEDF), and thus the electron transport coefficients and rate coefficients.[14] However, inclusion of the superelastic e-V collisions in nitrogen discharge simulations is rarely seen in the literature.[15,16]

In this study, we aim at the detailed fluid modeling of nitrogen DBD under an atmospheric-pressure condition, as driven by a realistic distorted sinusoidal AC (60 kHz) power source. In the modeling, we include the vibrationally excited nitrogen related reaction channels which are important in discharges. The simulated results are also compared with the experimental results wherever possible. The effects of the amplitude of the applied voltage, the dielectric thickness, and the dielectric materials on discharges are studied in the simulations.

2. Numerical Method

The fluid model is based on the solution of the electron continuity equation with the drift-diffusion approximation, the ion continuity equation with the drift-diffusion approximation, the neutral species continuity equation, the electron energy density equation, and Poisson's equation for an electrostatic distribution. These equations are summarized as follows:

$$\frac{\partial n_{e,i,n}}{\partial t} + \nabla \cdot \mathbf{\Gamma}_{e,i,n} = S_{e,i,n} \tag{1}$$

$$\mathbf{\Gamma}_{e,i} = -D_{e,i}\nabla n_{e,i} + n_{e,i}\mu_{e,i}\mathbf{E} \tag{2}$$

$$\mathbf{\Gamma}_n = -D_n\nabla n_n \tag{3}$$

*E-mail address: chongsin@faculty.nctu.edu.tw

© 2012 The Japan Society of Applied Physics

$$\frac{\partial}{\partial t}\left(\frac{3}{2}n_{\mathrm{e}}k_{\mathrm{B}}T_{\mathrm{e}}\right) + \nabla\cdot\left(\frac{5}{2}k_{\mathrm{B}}T_{\mathrm{e}}\boldsymbol{\Gamma}_{\mathrm{e}} - \frac{5}{2}\frac{n_{\mathrm{e}}k_{\mathrm{B}}T_{\mathrm{e}}}{m_{\mathrm{e}}v_{\mathrm{m}}}\nabla(k_{\mathrm{B}}T_{\mathrm{e}})\right)$$
$$= -e\boldsymbol{\Gamma}_{\mathrm{e}}\cdot\boldsymbol{E} - \varepsilon_{\mathrm{loss}} \qquad (4)$$

$$\nabla\cdot(\varepsilon\nabla\phi) = -\left(\sum_{i=1}^{K}q_i n_i - e n_{\mathrm{e}}\right), \qquad (5)$$

where n_{e}, n_{i}, n_{n}, $\boldsymbol{\Gamma}_{\mathrm{e}}$, $\boldsymbol{\Gamma}_{\mathrm{i}}$, and $\boldsymbol{\Gamma}_{\mathrm{n}}$ are the number densities and particle fluxes of electrons, ions, and neutrals with D_{e}, D_{i}, and D_{n} as the diffusion coefficients, respectively. μ_{e} and μ_{i} are the electron and ion mobilities, respectively. $\boldsymbol{E}$ is the electric field and $S_{\mathrm{e,i,n}}$ is the source or sink of each species associated with chemical reactions among various species. T_{e} is the electron temperature, k_{B} is the Boltzmann constant, m_{e} is the mass of an electron, and v_{m} is the momentum exchange collision frequency between electrons and background neutral particles. $\varepsilon_{\mathrm{loss}}$ includes the inelastic collision loss and elastic collision loss. ϕ is the electrostatic potential, and ε is the space-dependent permittivity, whose value is either the vacuum or dielectric permittivity depending upon the problem. Note that we neglect flow convection effects in this study. Drift and diffusion coefficients and rate constants related to electrons, which are functions of electron temperature, are obtained using the publicly available Boltzmann equation solver BOLSIG+.[17]

The boundary condition for the continuity equation of electrons is

$$\boldsymbol{\Gamma}_{\mathrm{e}} = \frac{1}{4}n_{\mathrm{e}}v_{\mathrm{th,e}} + \mu_{\mathrm{e}}n_{\mathrm{e}}\frac{\partial\phi}{\partial x} - D_{\mathrm{e}}\frac{\partial^2 n_{\mathrm{e}}}{\partial x^2} - \gamma\boldsymbol{\Gamma}_{\mathrm{i}}, \qquad (6)$$

where $\boldsymbol{\Gamma}_{\mathrm{e}}$ and $\boldsymbol{\Gamma}_{\mathrm{i}}$ are the electron and ion species fluxes, respectively, and $v_{\mathrm{th,e}}$ is the mean thermal velocity of electrons. Note that γ is the coefficient of secondary electron emission caused by ion bombardment on the surface. Since the secondary electron emission coefficient for metal electrodes is in the range from 0.01 to 0.1 and is expected to be much smaller for the dielectric surface, the emission coefficient was chosen to be equal to 10^{-4} for good agreement between simulations and experiments in the current study.

In this study, the above equations were recast into a one-dimensional (1D) form and discretized using the finite-difference method. The resulting system of nonlinear algebraic equations was solved using a fully implicit backward Euler's method in the temporal domain with the Scharfetter-Gummel scheme for the mass fluxes on the spatial domain. Details can be found in our previous work and are omitted here for brevity.[18]

3. Results and Discussion

3.1 Discharge structure

The atmospheric-pressure parallel-plate DBD consists of two electrodes ($5 \times 5\,\mathrm{cm}^2$), each covered by an alumina dielectric (95% Al_2O_3 with $\varepsilon = 12.63$) of 2 mm thickness. The distance between the two dielectric layers is 0.5 mm throughout the study. A distorted sinusoidal voltage waveform having a peak value of 6.6 kV with a frequency of 60 kHz was used to sustain the discharge throughout the study unless otherwise specified. A related experimental setup has been described in detail by Chiang *et al.*[3] and is not repeated here for brevity. Because the input voltage was not a sinusoidal waveform, it was fitted by a Fourier series

with 18 terms using 60 kHz as the fundamental frequency in the simulation. The N_2 plasma chemistry employed in the present study includes 11 species [electron, N, N(^{2}D), N_2, N_2^+, N_4^+, $N_2(X^1\Sigma_g^+$, $v = 1$–6), $N_2(A^3\Sigma_u^+)$, $N_2(B^3\Pi_g)$, $N_2(C^3\Pi_u)$, $N_2(a'^1\Sigma_u^-)$] and 34 reactions, which are summarized in Table I. Note that we have ignored N^+ and N_3^+ in the simulation since they have been found to be unimportant in nitrogen plasma simulations.[13] One hundred grid points and a time step of 5×10^{-10} are used for simulations throughout the study unless otherwise specified. Generally, 3–5 cycles of simulation are enough to reach a quasi-steady state solution. Only the data at the fourth cycle are presented for the purpose of discussion.

Figure 1 shows a comparison of simulated and measured discharged currents of nitrogen DBD along with an experimental photograph (0.2 s exposure time) of the discharge at the bottom. The homogeneous light emission justifies the use of 1D fluid modeling for this problem. Note that the various currents in the simulation are defined as follows:

$$J_{\mathrm{tot}}(t,x) = J_{\mathrm{displ}}(t,x) + J_{\mathrm{cond}}(t,x), \qquad (7)$$

$$J_{\mathrm{displ}}(t,x) = \varepsilon\frac{\partial E}{\partial t}, \qquad (8)$$

$$J_{\mathrm{cond}}(t,x) = \pm\Sigma e\Gamma_{\mathrm{e,N_2^+,N_4^+}}. \qquad (9)$$

Results show that simulated discharge currents are in good quantitative agreement with the experimental data throughout the cycle. The discharge current has the form of two major peaks per cycle and each peak has a duration of approximately 2 μs, in which the current intensity is about 10–20 mA/cm². In addition, the current peaks are much wider than the narrow peaks in helium discharges under similar conditions.[20]

Figure 2(a) shows the various spatially averaged current densities during a cycle. During the breakdown, the conduction currents are much higher than the displacement current, in which N_4^+ is dominant. In the post breakdown period, the displacement current is dominant, and the discharge is almost extinguished. Figure 2(b) shows the current continuity across the gap during the breakdown which is enforced in the 1D simulation as it should be.

Figure 3 shows the corresponding instantaneous distributions of discharge properties across the gap at the moment of peak current during the breakdown. It is observed that the electric field is almost linear (from 55 to 60 kV/cm) across the gap because of the low net charge density (difference between positive ions and electron), which is unlike a typical glow discharge with a quasi-neutral region. The number density of N_4^+ is much higher than that of electron across the gap. In addition, the electron number density decreases exponentially with increasing distance from the powered electrode (the anode on the left side). These results are similar to those of some earlier studies of atmospheric-pressure nitrogen discharges.[6,9,13] Interestingly, the density of N_2^+ species produced by directly ionized of electrons is two orders of magnitude lower than that of N_4^+ during the breakdown. Note that, the mechanism of conversion of the N_2^+ ion into the N_4^+ ion (reaction 19 in Table I) is very efficient.[13,15] It is also found that the electron energy density ($\varepsilon_{\mathrm{e}} = (3/2)n_{\mathrm{e}}kT_{\mathrm{e}}$) has peaks near the powered electrode because more electrons are attracted and generated. In addition, the electron temperature is close to 5 eV throughout the gap.

Table I. Summary of nitrogen plasma chemical reactions considered in the calculation.

| No.	Reaction channel	Threshold (eV)	Rate coefficient	Ref.
(1)	$e + N_2 \rightarrow e + N_2$	0.0	Cross section	17
(2)	$e + N_2 \rightarrow 2e + N_2^+$	15.58	Cross section	17
(3)	$e + N_2 \rightarrow e + N_2(\text{rot})$	0.02	Cross section	17
(4)	$e + N_2 \rightarrow e + N_2(\text{res})$	0.29	Cross section	17
(5)	$e + N_2 \rightarrow e + N_2(v=1)$	0.291	Cross section	17
(6)	$e + N_2 \rightarrow e + N_2(v=2)$	0.59	Cross section	17
(7)	$e + N_2 \rightarrow e + N_2(v=3)$	0.88	Cross section	17
(8)	$e + N_2 \rightarrow e + N_2(v=4)$	1.17	Cross section	17
(9)	$e + N_2 \rightarrow e + N_2(v=5)$	1.47	Cross section	17
(10)	$e + N_2 \rightarrow e + N_2(v=6)$	1.76	Cross section	17
(11)	$e + N_2 \rightarrow e + N_2(A^3\Sigma_u^+)$	6.17	Cross section	17
(12)	$e + N_2 \rightarrow e + N_2(B^3\Pi_g)$	7.35	Cross section	17
(13)	$e + N_2 \rightarrow e + N_2(a'^1\Sigma_u^-)$	8.40	Cross section	17
(14)	$e + N_2 \rightarrow e + N_2(C^3\Pi_u)$	11.03	Cross section	17
(15)	$e + N_2 \rightarrow e + 2N$	12.00	$1.25 \times 10^{-16} \times (11608 \times T_e)^{0.49}$ $\times \exp(-1.6 \times 10^5/11608/T_e)\,\text{m}^3\,\text{s}^{-1}$	24
(16)	$e + N_2^+ \rightarrow 2N$	0.0	$2.8 \times 10^{-13}(T_g/T_e)^{0.5}\,\text{m}^3\,\text{s}^{-1}$	6
(17)	$e + N_2^+ \rightarrow N(^2D) + N$	0.0	$3.7 \times 10^{-13}\,\text{m}^3\,\text{s}^{-1}$	25
(18)	$N_2^+ + N_2 + N_2 \rightarrow N_4^+ + N_2$	0.0	$5.0 \times 10^{-41}\,\text{m}^6\,\text{s}^{-1}$	15
(19)	$e + N_4^+ \rightarrow N_2(C^3\Pi_u) + N_2$	0.0	$2.0 \times 10^{-12}(T_g/T_e)^{0.5}\,\text{m}^3\,\text{s}^{-1}$	6
(20)	$N_2(a'^1\Sigma_u^-) + N_2(A^3\Sigma_u^+) \rightarrow e + N_4^+$	0.0	$5.0 \times 10^{-17}\,\text{m}^3\,\text{s}^{-1}$	13
(21)	$N_2(a'^1\Sigma_u^-) + N_2(a'^1\Sigma_u^-) \rightarrow e + N_4^+$	0.0	$2.0 \times 10^{-16}\,\text{m}^3\,\text{s}^{-1}$	13
(22)	$N_2(A^3\Sigma_u^+) + N_2(A^3\Sigma_u^+) \rightarrow N_2(B^3\Pi_g) + N_2$	0.0	$7.7 \times 10^{-17}\,\text{m}^3\,\text{s}^{-1}$	6
(23)	$N_2(A^3\Sigma_u^+) + N_2(A^3\Sigma_u^+) \rightarrow N_2(C^3\Pi_u) + N_2$	0.0	$3.0 \times 10^{-16}\,\text{m}^3\,\text{s}^{-1}$	6
(24)	$N_2(B^3\Pi_g) + N_2 \rightarrow N_2(A^3\Sigma_u^+) + N_2$	0.0	$5.0 \times 10^{-17}\,\text{m}^3\,\text{s}^{-1}$	6
(25)	$N_2(C^3\Pi_u) + N_2 \rightarrow N_2(a'^1\Sigma_u^-) + N_2$	0.0	$1.0 \times 10^{-17}\,\text{m}^3\,\text{s}^{-1}$	6
(26)	$N_2(a'^1\Sigma_u^-) + N_2 \rightarrow N_2(B^3\Pi_g) + N_2$	0.0	$2.0 \times 10^{-19}\,\text{m}^3\,\text{s}^{-1}$	6
(27)	$N_2(a'^1\Sigma_u^-) + N_2 \rightarrow 2N_2$	0.0	$2.0 \times 10^{-19}\,\text{m}^3\,\text{s}^{-1}$	6
(28)	$N + N + N_2 \rightarrow 2N_2$	0.0	$8.3 \times 10^{-46} \times \exp(500/T_g)\,\text{m}^6\,\text{s}^{-1}$	24
(29)	$N + N + N_2 \rightarrow N_2(A^3\Sigma_u^+) + N_2$	0.0	$8.27 \times 10^{-46} \times \exp(500/T_g)\,\text{m}^6\,\text{s}^{-1}$	24
(30)	$N + N + N_2 \rightarrow N_2(B^3\Pi_g) + N_2$	0.0	$8.3 \times 10^{-46} \times \exp(500/T_g)\,\text{m}^6\,\text{s}^{-1}$	24
(31)	$N_2(A^3\Sigma_u^+) \rightarrow N_2 + h\nu\ 293\,\text{nm}$	0.0	$5.0 \times 10^{-1}\,\text{s}^{-1}$	19
(32)	$N_2(B^3\Pi_g) \rightarrow N_2(A^3\Sigma_u^+) + h\nu\ 1045\,\text{nm}$	0.0	$1.5 \times 10^5\,\text{s}^{-1}$	19
(33)	$N_2(C^3\Pi_u) \rightarrow N_2(B^3\Pi_g) + h\nu\ 336.5\,\text{nm}$	0.0	$2.7 \times 10^7\,\text{s}^{-1}$	19
(34)	$N_2(a'^1\Sigma_u^-) \rightarrow N_2 + h\nu\ 177.1\,\text{nm}$	0.0	$1.0 \times 10^2\,\text{s}^{-1}$	19
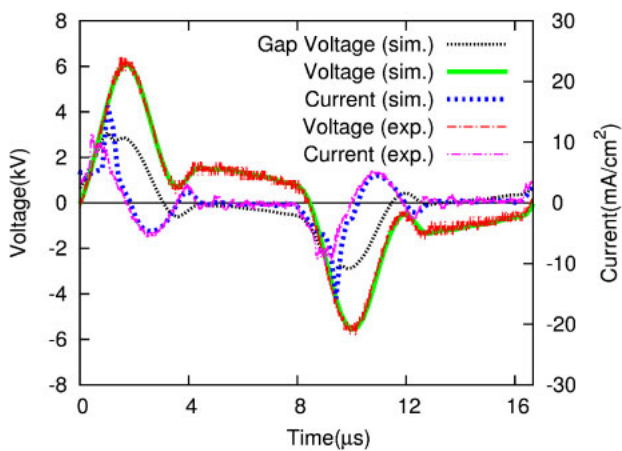
Fig. 1. (Color online) Comparison between simulated and experimental current–voltage characteristics at a voltage of 6600 V and a frequency of 60 kHz. The distance between the two dielectric layers is 0.5 mm and the dielectric is 2.0 mm alumina. A photograph of discharge at the bottom acquired with 0.2 exposed time.

Figure 4 shows instantaneous distributions of discharge properties across the gap at the moment of negligible current after the breakdown. N_4^+ ($\sim 10^{14}\,\text{m}^{-3}$) is also found to be the most dominant charged species at this moment, but the density is two orders of magnitude smaller than that during the breakdown period, as shown in Fig. 3. This is caused by the continuing associated ionization between the remaining long-lived metastable nitrogen species (reactions 20 and 21 in Table I). In addition, the number densities of N_2^+ and electrons become as low $\sim 10^8$ and $\sim 10^{11}\,\text{m}^{-3}$, respectively, because there is no direct ionization at this moment. This is mainly because the electron energy density becomes much lower, ~ 4 orders of magnitude lower with an electron temperature of $\sim 2\,\text{eV}$, than that in the breakdown period, which leads to indirect ionization in this post breakdown period.

3.2 Influence of external driving voltage
Figure 5 shows the cycle-space averaged number densities of various species with peak voltages in the range of 6.2–8.6 kV with a gap distance of 0.5 mm and two ceramic layers
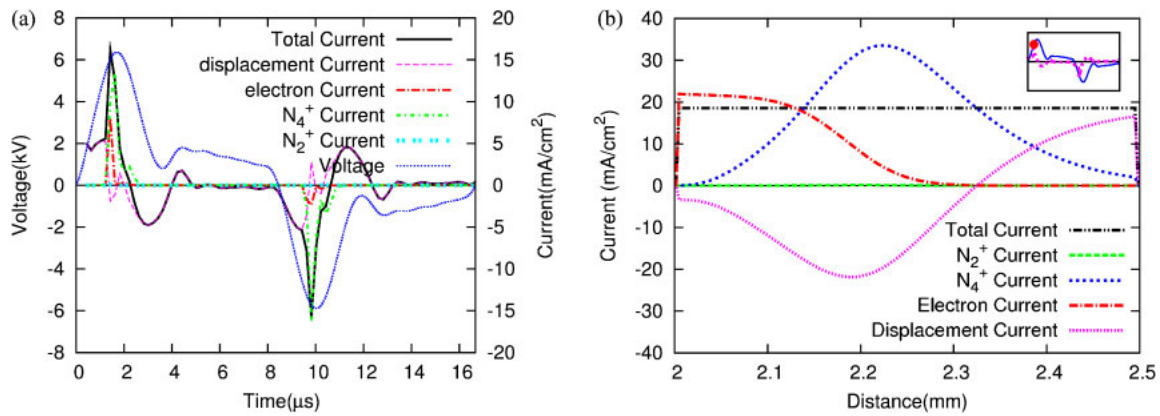
Fig. 2. (Color online) Distributions of various discharge currents (a) during a cycle (b) at the maximum discharge current obtained via numerical modeling. The gap distance is 0.5 mm and a 2.0 mm thick alumina dielectric is used. The applied voltage is 6600 V and the frequency is 60 kHz.
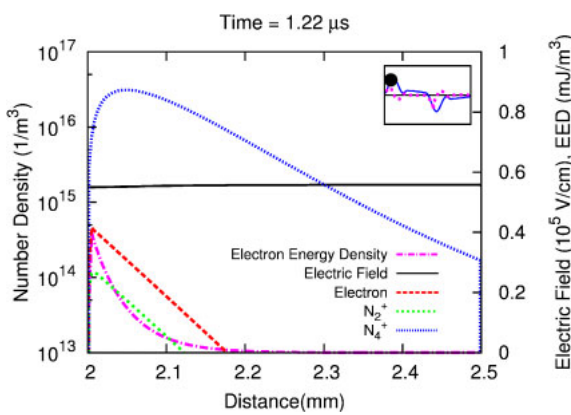

Fig. 3. (Color online) Spatial distributions of electric field, charged particles, and electron energy density at the time of maximum discharge current (1.22 μs) between two alumina dielectric materials. The operating conditions are the same as those indicated in Fig. 1.
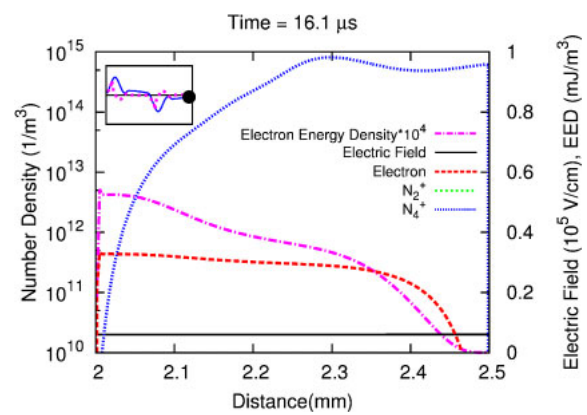

Fig. 4. (Color online) Spatial distributions of electric field, charged particles, and electron energy density at 16.1 μs (after the breakdown) between two alumina dielectric materials. The operating conditions are the same as those indicated in Fig. 1.
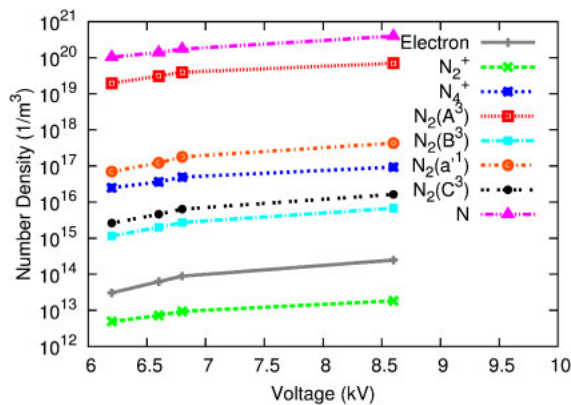

Fig. 5. (Color online) Cycle-space averaged number densities of various species in nitrogen DBD at various applied voltages of 6200, 6600, 6800, 8600 V, and a fixed gap distance of 0.5 mm. The alumina dielectric thickness is 2.0 mm and the frequency is 60 kHz for all cases.

Table II. Comparison of average absorbed powers at various applied voltages of 6200, 6600, 6800, and 8600 V in a 60 kHz cycle and a fixed gap distance of 0.5 mm.

Voltage (V)	Electrons absorbed (W/cm³)	N_2^+ absorbed (W/cm³)	N_4^+ absorbed (W/cm³)	Total absorbed (W/cm³)
6200	1.40	0.035	15.65	17.09
6600	4.99	0.076	40.11	45.18
6800	5.35	0.091	46.48	51.92
8600	21.39	0.244	121.98	143.61

of 2.0 mm thickness. Generally, the number densities of all species increase exponentially with the magnitude of applied peak voltage. The ion density ($\sim 10^{16}$ m^{-3}) is three orders of magnitude higher than the electron density ($\sim 10^{13}$ m^{-3}). The metastable species $N_2(A^3\Sigma_u^+)$ and atomic nitrogen are the most dominant species with number densities of 10^{19}–10^{21} m^{-3}, which agree reasonably well with the experimental measurements.[21,22] It should be noted that the number densities of all species increase with increasing applied voltage; however, the dielectric material may become more vulnerable with increasing applied voltage. Table II shows a summary of the average absorbed powers of electron and ions at different applied peak voltages. The power absorbed by electrons is generally one order of magnitude smaller than the power absorbed by N_4^+. This is unlike most glow-like discharges driven by RF power sources, in which most of the electric power is absorbed by the electrons instead. However, gas heating often increases with increasing power absorbed by ion owing to the efficient energy transfer between ions and background neutrals.[23]
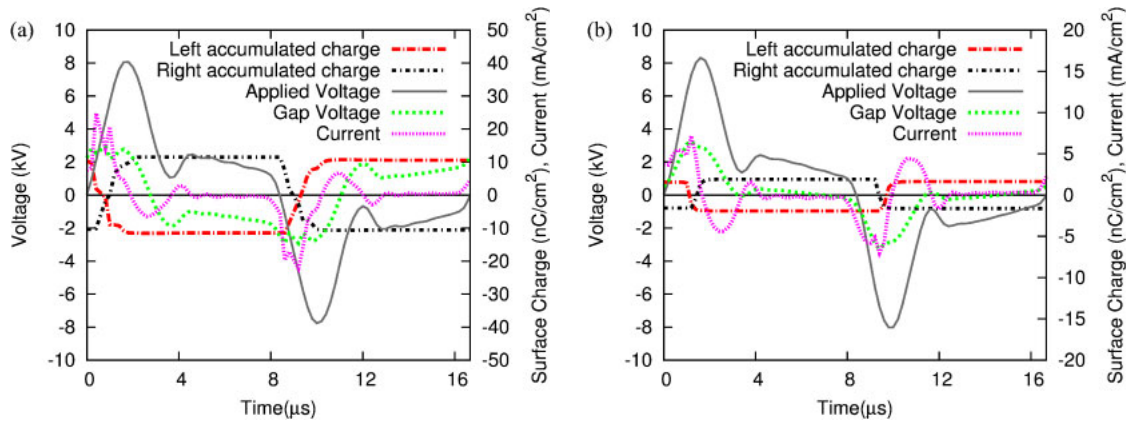
Fig. 6. (Color online) Simulated current, gap voltage, applied voltage, and accumulated charges at dielectric surfaces of different dielectric materials: (a) 2.0 mm ceramic and (b) 2.0 mm quartz. The applied peak voltage is 8600 V and the frequency is 60 kHz. The gap distance between dielectric materials is kept at 0.5 mm.

Table III. Comparisons of average number density, electron temperature and total absorbed power between ceramic dielectrics of thicknesses 1.0 and 2.0 mm, at 6200 V applied voltage and 60 kHz frequency.

Dielectric thickness (mm)	Electron density (m^{-3})	N_2^+ density (m^{-3})	N_4^+ density (m^{-3})	$N_2(A^3)$ density (m^{-3})	$N_2(a'^1)$ density (m^{-3})	Electron absorbed (W/cm^3)	N_2^+ absorbed (W/cm^3)	N_4^+ absorbed (W/cm^3)
1.0	6.08×10^{14}	1.68×10^{13}	8.15×10^{16}	6.47×10^{19}	3.80×10^{17}	21.99	0.213	119.80
2.0	3.04×10^{13}	4.91×10^{12}	2.49×10^{16}	1.97×10^{19}	7.01×10^{16}	1.40	0.035	15.65

3.3 Influence of dielectric material

Figures 6(a) and 6(b) show the discharge current, gap voltage, and accumulated charges on the surfaces of materials of ceramic ($\varepsilon = 12.63$) and quartz ($\varepsilon = 4.76$) dielectric materials of 2.0 mm thickness, respectively. The gap distance between the dielectric materials is maintained at 0.5 mm. The applied peak voltage is 8,600 V, which can sustain the nitrogen DBD with two quartz dielectrics using a power source with a frequency of 60 kHz. Results show that the larger the permittivity of the dielectric material, the larger the discharge current and the longer the period. In addition, the quantity of accumulated charges at each electrode increases with increasing permittivity of the dielectric material. It is especially important that accumulated negative charges at the dielectric surface prevent arc occurrence in nitrogen DBD by decreasing the gap voltage on the powered side. These results coincide with those obtained previously by Golubovskii *et al.*,[7] who also showed that larger applied voltage is required to sustain the discharge when the permittivity is smaller.

3.4 Influence of thickness of dielectric layer

Table III shows a summary of the average number densities and absorbed power at two different thicknesses of the ceramic layer (1.0 and 2.0 mm). Simulation conditions include a gap distance of 0.5 mm, an applied peak voltage of 6,200 V, and a frequency of 60 kHz. Results show that the average number densities and the power absorbed by plasma decrease dramatically with increasing thickness. Note that the discharge for a ceramic layer of 1 mm thickness is much easier to sustain in the experiments, but the operating voltage peak is limited to 6.4 kV without damage. As the thickness increases up to 2.0 mm, the ceramic can survive the peak voltage up to

9.0 kV. Table III shows that as the dielectric thickness decreased from 2.0 to 1.0 mm, the density and power absorption of N_4^+ increased by almost one order of magnitude.

4. Conclusions

In the present study, we have investigated in detail the non-equilibrium atmospheric-pressure nitrogen dielectric barrier discharge driven by a realistic distorted-sinusoidal voltage power source (60 kHz) using a self-consistent 1D fluid modeling code considering non-local electron energy transport (local mean energy approximation). The simulated discharge currents in a benchmark test case agree very well with the experimental data. During the breakdown, the conduction current is much higher than the displacement current, in which N_4^+ is the dominating charged species. The discharge absorbs electric power mainly through the moving ions, rather than the electrons, which is unlike most glow discharges driven by RF power sources. The densities of all species increase exponentially with increasing applied peak voltage in the range of 6.2–8.6 kV, in which the metastable $N_2(A^3\Sigma_u^+)$ and atomic nitrogen are found to be the most dominant species. Species densities increase exponentially with the magnitude of applied peak voltage. The higher permittivity of the dielectric material, the larger the discharge current and the longer the breakdown period. Finally, the increase in dielectric thickness from 1.0 to 2.0 mm greatly reduces the densities of all species and also the power absorbed by the plasma.

1) U. Kogelschatz: Plasma Chem. Plasma Process. **23** (2003) 1.
2) H. E. Wagner, R. Brandenburg, K. V. Kozlov, A. Sonnenfeld, P. Michel, and J. F. Behnke: Vacuum **71** (2003) 417.
3) M. H. Chiang, K. C. Liao, I. M. Lin, C. C. Lu, H. Y. Huang, C. L. Kuo, J. S. Wu, C. C. Hsu, and S. H. Chen: Plasma Chem. Plasma Process. **30** (2010) 553.
4) J. Tepper and M. Lindmayer: Proc. Contrib. Pap. 7th Int. Symp. High Pressure Low Temperature Plasma Chemistry, 2000, p. 38.
5) Y. B. Golubovskii, V. A. Maiorov, J. F. Behnke, J. Tepper, and M. Lindmayer: J. Phys. D **37** (2004) 1346.
6) Y. H. Choi, J. H. Kim, and Y. S. Hwang: Thin Solid Films **506–507** (2006) 389.
7) Y. B. Golubovskii, V. A. Maiorov, P. Li, and M. Lindmayer: J. Phys. D **39** (2006) 1574.
8) V. A. Maiorov and Y. B. Golubovskii: Plasma Sources Sci. Technol. **16** (2007) S67.
9) F. Massines, N. Gherardi, N. Naudé, and P. Ségur: Eur. Phys. J.: Appl. Phys. **47** (2009) 22805.
10) K. W. Cheng, C. T. Hung, M. H. Chiang, F. N. Hwang, and J. S. Wu: Comput. Phys. Commun. **182** (2011) 164.
11) H. C. Kim, F. Isa, S. S. Yang, M. Radmilović-Radjenović, and J. K. Lee: J. Phys. D **38** (2005) R283.
12) G. K. Grubert, M. M. Becker, and D. Loffhagen: Phys. Rev. E **80** (2009) 036405.
13) Y. B. Golubovskii, V. A. Maiorov, J. Behnke, and J. F. Behnke: J. Phys. D **35** (2002) 751.
14) J. Loureiro and C. M. Ferreira: J. Phys. D **19** (1986) 17.
15) E. Panousis, L. Papageorghiou, N. Spyrou, J. F. Loiseau, B. Held, and F. Clément: J. Phys. D **40** (2007) 4168.
16) E. Panousis, A. Ricard, J. F. Loiseau, F. Clément, and B. Held: J. Phys. D **42** (2009) 205201.
17) Bolsig [http://www.siglo-kinema.com/bolsig.htm].
18) C. T. Hung, Y. M. Chiu, F. N. Hwang, and J. S. Wu: Comput. Phys. Commun. **182** (2011) 161.
19) M. Capitelli, C. M. Ferreira, B. F. Gordiets, and A. I. Osipov: *Plasma Kinetics in Atmospheric Gases* (Springer, Berlin, 2000) p. 157.
20) F. Massines, A. Rabehi, P. Decomps, R. B. Gadri, P. Ségur, and C. Mayoux: J. Appl. Phys. **83** (1998) 2950.
21) G. Dilecce, P. F. Ambrico, and S. D. Benedictis: Plasma Sources Sci. Technol. **16** (2007) 511.
22) E. Panousis, A. Ricard, J. F. Loiseau, F. Clément, and B. Held: J. Phys. D **42** (2009) 205201.
23) S. Y. Jou, C. T. Hung, Y. M. Chiu, J. S. Wu, and B. Y. Wei: Plasma Chem. Plasma Process. **30** (2010) 907.
24) I. H. Tsai and C. C. Hsu: IEEE Trans. Plasma Sci. **38** (2010) 3387.
25) F. Tochikubo, S. Uchida, H. Yasui, and K. Sato: Jpn. J. Appl. Phys. **48** (2009) 076507.